PHYSICAL REVIEW B **96**, 155430 (2017)

Multiband k · p theory of monolayer XSe (X=In, Ga)

Ma Zhou,[1,2] Rui Zhang,[1,2] Jiangpeng Sun,[1,2] Wen-Kai Lou,[1,2] Dong Zhang,[1,2] Wen Yang,[3] and Kai Chang[1,2,*]

[1]*SKLSM, Institute of Semiconductors, Chinese Academy of Sciences, P.O. Box 912, Beijing 100083, China*

[2]*College of Materials Science and Opto-Electronic Technology, University of Chinese Academy of Sciences, Beijing 100049, China*

[3]*Beijing Computational Science Research Center, Beijing 100193, China*

(Received 17 July 2017; published 11 October 2017)

We derive the multiband **k** · **p** Hamiltonian for an electron in monolayer XSe (X = In, Ga) near the Γ point in the presence of spin-orbit coupling and strain. With four conduction bands and ten valence bands included, the 14-band **k** · **p** Hamiltonian is capable of describing the nonparabolic energy band dispersion, strong interband mixing, and strain-induced effects, in good agreement with first-principles calculations. This **k** · **p** theory provides a simple and convenient way to understand and manipulate the optical and transport properties of monolayer XSe and their nanostructures by strain and external fields. Interestingly, we find that uniaxial strain can even induce an indirect-to-direct band-gap transition in these two-dimensional materials.

DOI: 10.1103/PhysRevB.96.155430

I. INTRODUCTION

The discovery of graphene has triggered a great leap in the research on monolayer two-dimensional (2D) materials [1]. A decade of intense research on fabricating 2D atomic crystals has revealed many three-dimensional van der Waals solids, e.g., transition metal dichalcogenides [2–6] and phosphorus [7–10] can be exfoliated down to monolayer thickness. Recently, a high-quality few-layer InSe encapsulated in hexagonal boron nitride under an inert atmosphere was reported [11]. This explosion of experimental results aroused researcher enthusiasm for III to VI semiconductors again.

Layered III to VI semiconductors have attracted much attention for their intrinsic outstanding properties and potential application in nonlinear optics [12–22]. The electronic band structures of layered compounds GaSe and InSe have been investigated by first-principles calculations [18] and the tight-binding approach [19]. In the case of layered InSe, photoluminescence measurements under pressure reveal that high pressure can induce an unconventional direct-indirect band gap transition [20,21]. Its 2D counterparts become the next generation of graphenelike materials. Including an InSe monolayer [11], the metal monochalcogenides monolayer GaSe, and GaS, have been successfully synthesized [23–29]. Recently, atomically thin GaSe nanosheets were prepared by exfoliation and were deemed to be a promising material for high performance photodetectors [23]. In the same year, transistor characteristics based on single sheets of GaS and GaSe have been measured [26]. Besides exfoliation, large-area few-layer GaSe crystals were successfully grown on insulating substrates using the vapor phase transport method [27]. As predicted by first-principles calculations [30], the conduction band bottoms of XSe (X = Ga, In) and GaS locate at the Γ and M points, respectively. Thus the physical properties of XSe (GaS) are dominated by the electronic states near the Γ (M) point.

Very recently the monolayer and few-layer groups III to VI metal monochalcogenide XSe (X = Ga, In) has been studied based on first-principles calculations [30–32], the tight-binding model [33], and the single-band **k** · **p** model [33,34]. When the thickness of GaSe and InSe decreases, the band gap of GaSe and InSe changes from a direct gap to an indirect gap at a critical thickness [32], as opposed to the indirect-to-direct band-gap transition of transition-metal dichalcogenides when its thickness decreases to a single monolayer [32]. The presence of saddle points along the Γ-M line leads to a Lifshitz transition in the case of hole doping [31]. These studies provide important information about the electronic structure and physical properties of monolayer XSe. However, they still suffer from a few limitations. First, although the first-principles calculations and the tight-binding model provide accurate descriptions for monolayer XSe, however, it is difficult to establish a simple physical picture to understand and manipulate their electronic structures and physical properties by various external magnetic fields and strain. Moreover, these atomistic approaches become inefficient in describing nanostructures consisting of these materials due to the large supercells involved. Second, the existing tight-binding model neglects the strong spin-orbit coupling effect, which is necessary to understand the valence band structure and spin-related properties of XSe. Third, a most interesting feature of XSe is the strong interband mixing and the resulting sombrero shape of the top valence band near the Γ point. Although the single-band **k** · **p** model [34] provides a description for the sombrero dispersion, it cannot describe either the intrinsic interband coupling or the effect of strain or external fields, which can change the band dispersions significantly.

In this paper, we adopt the standard invariant theory to derive a general 14-band (including the spin degree of freedom) **k** · **p** Hamiltonian for the electronic structure of monolayer XSe (X = In, Ga) near the Γ point in the presence of spin-orbit coupling and strain. With four conduction bands and ten valence bands in the vicinity of the band gap included, our **k** · **p** Hamiltonian can describe not only the nonparabolic dispersion near the Γ point, but also the strong interband mixing and strain effects, in good agreement with first-principles calculations. This can provide a clear physical picture and an efficient way to understand and manipulate the electronic and optical properties of monolayer XSe and their nanostructures (such as quantum dots and nanoribbons) by strain and external fields for device applications. In particular

*Corresponding author: kchang@semi.ac.cn

for the InSe monolayer, we find that uniaxial strain can be utilized to change the indirect band gap to a direct gap. The invariant expansion method and our multiband model can also be extended to few-layer systems.

The rest of this paper is organized as follows. In Sec. II, we adopt the standard invariant theory to derive the 14-band $\mathbf{k}\cdot\mathbf{p}$ Hamiltonian for XSe monolayer incorporating the spin-orbit coupling effects. In Sec. III, we further consider the strain effect and demonstrate the strain-induced indirect-to-direct band-gap transition. Finally, in Sec. IV, we give a brief conclusion.

II. 14-BAND k · p HAMILTONIAN OF MONOLAYER METAL CHALCHGENIDES

As shown in Fig. 1(a), the unit cell of the monolayer XSe (X = In or Ga) consists of four ions in two sublayers, with one indium (or gallium) and one selenium in each sublayer. The point group of monolayer XSe is D_{3h}, which consists of 12 symmetry operations divided into six classes and hence six *real*, irreducible representations (see Table I). As shown in Fig. 1(d), in the absence of spin-orbit coupling (SOC), the transport and optical properties of monolayer XSe are dominated by seven energy bands (or 14 energy bands if the spin degree of freedom is included) in the vicinity of the Fermi level [32]. Their orbital wave functions at the Γ point are (ordered with decreasing energy):

$$\begin{aligned}|\Psi_{1c}\rangle &\sim 1,\\ |\Psi_{4}\rangle &\sim z,\\ |\Psi_{1v}\rangle &\sim 1,\\ |\Psi_{5}\rangle \equiv (|\Psi_{5,x}\rangle,|\Psi_{5,y}\rangle) &\sim (R_x,R_y),\\ |\Psi_{6}\rangle \equiv (|\Psi_{6,x}\rangle,|\Psi_{6,y}\rangle) &\sim (x,y),\end{aligned}$$

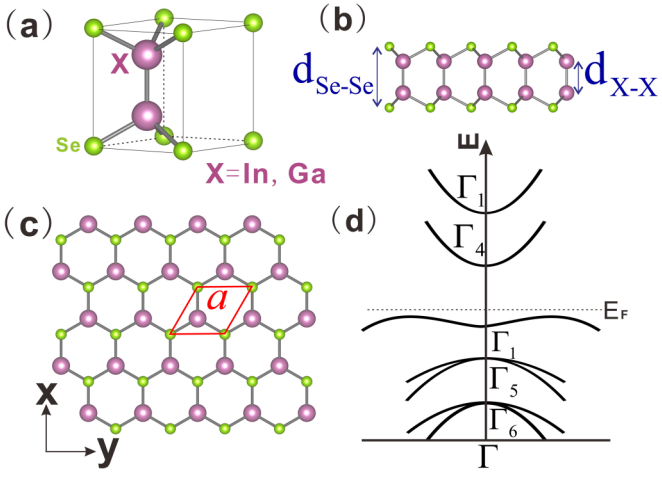

FIG. 1. (a) Schematic of the primitive cell of an XSe monolayer (X = In, Ga). (b) and (c) are side and top views, respectively, of the hexagonal structure. The purple and green spheres correspond to X and selenium atoms, respectively. The x and y axes along zigzag and armchair directions specify the coordinates used in the $\mathbf{k}\cdot\mathbf{p}$ Hamiltonian. (d) A sketch of the monolayer InSe electronic bands around the Γ point, omitting the spin-orbit coupling. E_F is the Fermi Energy.

TABLE I. Character table of group D_{3h} and the basis functions for each irreducible representation. Here (x,y,z) and (x',y',z') are the three Cartesian components of an ordinary vector (that changes sign under spatial inversion) and (R_x,R_y,R_z) are the three Cartesian components of an axial vector (that remains invariant under spatial inversion).

D_{3h}	E	σ_h	$2C_3$	$2S_3$	$3C'_{2i}$	$3\sigma_{vi}$	Basis functions
Γ_1	1	1	1	1	1	1	1 or $xx'+yy'$ or zz'
Γ_2	1	1	1	1	−1	−1	R_z or $xy'-yx'$
Γ_3	1	−1	1	−1	1	−1	zR_z
Γ_4	1	−1	1	−1	−1	1	z
Γ_5	2	−2	−1	1	0	0	(R_x,R_y)
Γ_6	2	2	−1	−1	0	0	(x,y) or $(yy'-xx',xy'+yx')$

where the symbol "∼" tells us how these basis functions transform under D_{3h} operations, e.g., $|\Psi_{1c}\rangle$ and $|\Psi_{1v}\rangle$ remain invariant under all D_{3h} operations, $|\Psi_6\rangle$ transform like the two transverse components (x,y) of an ordinary vector (which changes sign under spatial inversion), while $|\Psi_5\rangle$ transform like the two transverse components (R_x,R_y) of an axial vector (which remains invariant under spatial inversion).

In the basis $|\Psi_{1c}\rangle,|\Psi_{1v}\rangle,|\Psi_6\rangle,|\Psi_4\rangle,|\Psi_5\rangle$, the $\mathbf{k}\cdot\mathbf{p}$ Hamiltonian assumes the 5×5 block form:

$$\mathbf{H}=\left[\begin{array}{ccc|cc}\mathbf{H}^{1c,1c} & \mathbf{H}^{1c,1v} & \mathbf{H}^{1c,6} & \mathbf{H}^{1c,4} & \mathbf{H}^{1c,5}\\ \mathbf{H}^{1v,1c} & \mathbf{H}^{1v,1v} & \mathbf{H}^{1v,6} & \mathbf{H}^{1v,4} & \mathbf{H}^{1v,5}\\ \mathbf{H}^{6,1c} & \mathbf{H}^{6,1v} & \mathbf{H}^{6,6} & \mathbf{H}^{6,4} & \mathbf{H}^{6,5}\\ \hline \mathbf{H}^{4,1c} & \mathbf{H}^{4,1v} & \mathbf{H}^{4,6} & \mathbf{H}^{4,4} & \mathbf{H}^{4,5}\\ \mathbf{H}^{5,1c} & \mathbf{H}^{5,1v} & \mathbf{H}^{5,6} & \mathbf{H}^{5,4} & \mathbf{H}^{5,5}\end{array}\right],$$

where $\mathbf{H}^{\alpha\beta}$ is the block matrix between $|\Psi_\alpha\rangle$ and $|\Psi_\beta\rangle$, e.g., $\mathbf{H}^{1c,1c}$ is a 1×1 block matrix associated with $|\Psi_{1c}\rangle$, $\mathbf{H}^{6,6}$ is a 2×2 block matrix associated with $|\Psi_6\rangle$, and $\mathbf{H}^{1c,6}$ is a 1×2 block matrix associated with the coupling between $|\Psi_{1c}\rangle$ and $|\Psi_6\rangle$. Under mirror reflection σ_h about the xy plane, the basis states $|\Psi_{1c}\rangle,|\Psi_{1v}\rangle,|\Psi_6\rangle$ have even parity, while the other basis states have odd parity (see Table I); thus the $\mathbf{k}\cdot\mathbf{p}$ Hamiltonian can also be written as

$$\mathbf{H}=\begin{bmatrix}\mathbf{H}^{e-e} & \mathbf{H}^{e-o}\\ \mathbf{H}^{o-e} & \mathbf{H}^{o-o}\end{bmatrix},$$

where $\mathbf{H}^{e-e}$ is the 4×4 block matrix describing the coupling between the even-parity bands, $\mathbf{H}^{o-o}$ is the 3×3 block matrix describing the coupling between the odd-parity bands, and $\mathbf{H}^{o-e}=(\mathbf{H}^{e-o})^\dagger$ describes the coupling between the energy bands of opposite parities. Each matrix element of the $\mathbf{k}\cdot\mathbf{p}$ Hamiltonian is still a function of certain operators (denoted by $\mathcal{K}$) acting on the "slow" degree of freedom (whose Fourier components lie within the first Brillouin zone), such as the momentum operator $\mathbf{k}$, the spin operator $\mathbf{s}$, slowly varying external electric field $\mathbf{E}$, magnetic field $\mathbf{B}$, or strain tensor ϵ; thus we denote the $\mathbf{k}\cdot\mathbf{p}$ Hamiltonian by $\mathbf{H}(\mathcal{K})$.

A. Theory of invariants

The theory of invariants [35–38] provides a standard, systematic approach to construct the $\mathbf{k}\cdot\mathbf{p}$ Hamiltonian based on the invariance of the crystal Hamiltonian $\hat{H}$ under all operations of the symmetry group D_{3h} and its connection to

the $\mathbf{k}\cdot\mathbf{p}$ Hamiltonian within the energy bands of interest: $\hat{H}=\sum_{\alpha,\beta}|\Psi_\alpha\rangle\langle\Psi_\beta|\otimes\mathbf{H}^{\alpha\beta}(\mathcal{K})$. This equation decomposes the crystal Hamiltonian into the "fast" degree of freedom $|\Psi_\alpha\rangle\langle\Psi_\beta|$ and the "slow" degree of freedom $\mathbf{H}^{\alpha\beta}(\mathcal{K})$. Under an arbitrary symmetry operation $g\in \mathrm{D_{3h}}$, the basis $|\Psi_\alpha\rangle$ transforms according to the irreducible representation Γ_α, so the invariance of the crystal Hamiltonian under the symmetry operation g dictates

$$\mathbf{D}^{\alpha}(g)\mathbf{H}^{\alpha\beta}\big(\hat{P}_g\mathcal{K}\hat{P}_g^{-1}\big)\mathbf{D}^{\beta}(g^{-1})=\mathbf{H}^{\alpha\beta}(\mathcal{K}), \tag{1}$$

where $\mathbf{D}^{\alpha}(g)$ is the representation matrix of g in Γ_α and $\hat{P}_g\mathcal{K}\hat{P}_g^{-1}$ denotes the transformation of $\mathcal{K}$ under the operation g, e.g., if g is a $\pi/2$ rotation around the z axis and $\mathcal{K}$ is the 2D momentum operator, then $\hat{P}_g(k_x,k_y)\hat{P}_g^{-1}=(k_y,-k_x)$.

The general expression of an arbitrary block $\mathbf{H}^{\alpha\beta}(\mathcal{K})$ of the $\mathbf{k}\cdot\mathbf{p}$ Hamiltonian can be constructed in three steps [39]:

(i) Reducing the direct-product representation $\Gamma_\alpha\otimes\Gamma_\beta^*$ into irreducible representations $\oplus_\gamma\Gamma_\gamma$, where $\Gamma_\beta^*=\Gamma_\beta$ since all the irreducible representations of $\mathrm{D_{3h}}$ are real.

(ii) For each irreducible representation Γ_γ, construct the invariant

$$\mathbf{I}_\gamma^{\alpha\beta}(\mathcal{K})=\sum_l \mathbf{X}_{\gamma,l}^{\alpha,\beta}\mathcal{K}_{\gamma,l} \tag{2}$$

that satisfies Eq. (1). Here $\{\mathcal{K}_{\gamma,l}\}$ are irreducible tensor operators that are constructed from the operators $\mathcal{K}$ and transform under $\mathrm{D_{3h}}$ operations according to the lth column of Γ_γ, i.e., $\hat{P}_g\mathcal{K}_{\gamma,l}\hat{P}_g^{-1}=\sum_{l'}\mathcal{K}_{\gamma,l'}D^{\gamma}_{l'l}(g)$, while $\{\mathbf{X}_{\gamma,l}^{\alpha,\beta}\}$ are symmetrized matrices that have the same dimensions as $\mathbf{H}^{\alpha\beta}$ and transform under $\mathrm{D_{3h}}$ operations according to the lth column of Γ_γ, i.e., $\mathbf{D}^{\alpha}(g)\mathbf{X}_{\gamma,l}^{\alpha,\beta}\mathbf{D}^{\beta}(g^{-1})=\sum_{l'}\mathbf{X}_{\gamma,l'}^{\alpha,\beta}D^{\gamma}_{l'l}(g)$.

(iii) $\mathbf{H}^{\alpha\beta}(\mathcal{K})$ is given by a general linear combination of all these invariants:

$$\mathbf{H}^{\alpha\beta}(\mathcal{K})=\sum_\gamma c_\gamma^{\alpha\beta}\mathbf{I}_\gamma^{\alpha\beta}(\mathcal{K}). \tag{3}$$

In addition to the point group symmetry, the time-reversal symmetry imposes extra constraints on the $\mathbf{k}\cdot\mathbf{p}$ Hamiltonian. For XSe, if we can take all the basis functions to be real and hence invariant under time reversal, then the time-reversal invariance of the crystal Hamiltonian $\hat{\theta}\hat{H}\hat{\theta}^{-1}=\hat{H}$ dictates the time-reversal invariance of the $\mathbf{k}\cdot\mathbf{p}$ Hamiltonian: $\hat{\theta}\mathbf{H}(\mathcal{K})\hat{\theta}^{-1}=\mathbf{H}(\mathcal{K})$, where $\hat{\theta}$ is the time-reversal operator. Under time reversal, the momentum operator $\mathbf{k}$, the spin operator $\mathbf{s}$, and the magnetic field $\mathbf{B}$ have odd parity (i.e., they change sign), while the strain tensor ϵ and the electric field $\mathbf{E}$ have even parity (i.e., they remain invariant). In terms of the invariant expansion Eqs. (2) and (3), time-reversal symmetry dictates each invariant to have an even parity under time-reversal. Without loosing generality, we choose the coefficients $\{c_\gamma\}$ in Eq. (3) to be real. Then in Eq. (2), the symmetrized matrix $\mathbf{X}_{\gamma,l}^{\alpha,\beta}$ should have the same parity as the irreducible operator $\mathcal{K}_{\gamma,l}$ under time reversal: if $\hat{\theta}\mathcal{K}_{\gamma,l}\hat{\theta}^{-1}=\mathcal{K}_{\gamma,l}$, then $\mathbf{X}_{\gamma,l}^{\alpha,\beta}$ must be real; if $\hat{\theta}\mathcal{K}_{\gamma,l}\hat{\theta}^{-1}=-\mathcal{K}_{\gamma,l}$, then $\mathbf{X}_{\gamma,l}^{\alpha,\beta}$ must be purely imaginary. Finally, the $\mathbf{k}\cdot\mathbf{p}$ Hamiltonian must be Hermitian; this dictates that the invariants for a diagonal block must be Hermitian: $\mathbf{I}_\gamma^{\alpha\alpha}(\mathcal{K})=[\mathbf{I}_\gamma^{\alpha\alpha}(\mathcal{K})]^\dagger$.

TABLE II. Symmetrized matrices for the monolayer XSe, where $\mathbb{I}_{2\times2}$ denotes the 2×2 identity matrix, τ_x,τ_y,τ_z are Pauli matrices acting on the orbital band-edge Bloch states, $\Lambda_+=[1,0]$, $\Lambda_-=[0,1]$, $\mathbf{H}^{1,1}$ stands for $\mathbf{H}^{1c,1c}$,$\mathbf{H}^{1v,1v}$,$\mathbf{H}^{1c,1v}$,$\mathbf{H}^{1v,1c}$, and $\mathbf{H}^{1,4}$ stands for $\mathbf{H}^{1c,4}$,$\mathbf{H}^{1v,4}$, etc.

$\mathbf{H}^{1,1}$	$\Gamma_1\otimes\Gamma_1^*=\Gamma_1$	$\Gamma_1:1$
$\mathbf{H}^{4,4}$	$\Gamma_4\otimes\Gamma_4^*=\Gamma_1$	$\Gamma_1:1$
$\mathbf{H}^{1,4}$	$\Gamma_1\otimes\Gamma_4^*=\Gamma_4$	$\Gamma_4:1$
$\mathbf{H}^{1,5}$	$\Gamma_1\otimes\Gamma_5^*=\Gamma_5$	$\Gamma_5:(\Lambda_-,-\Lambda_+)$
$\mathbf{H}^{4,6}$	$\Gamma_4\otimes\Gamma_6^*=\Gamma_5$	$\Gamma_5:(\Lambda_-,-\Lambda_+)$
$\mathbf{H}^{1,6}$	$\Gamma_1\otimes\Gamma_6^*=\Gamma_6$	$\Gamma_6:(\Lambda_+,\Lambda_-)$
$\mathbf{H}^{4,5}$	$\Gamma_4\otimes\Gamma_5^*=\Gamma_6$	$\Gamma_6:(\Lambda_+,\Lambda_-)$
$\mathbf{H}^{5,5}$	$\Gamma_5\otimes\Gamma_5^*=\Gamma_1\oplus\Gamma_2\oplus\Gamma_6$	$\Gamma_1:\mathbb{I}_{2\times2}$ $\Gamma_2:\tau_y$ $\Gamma_6:(\tau_z,-\tau_x)$
$\mathbf{H}^{6,6}$	$\Gamma_6\otimes\Gamma_6^*=\Gamma_1\oplus\Gamma_2\oplus\Gamma_6$	$\Gamma_1:\mathbb{I}_{2\times2}$ $\Gamma_2:\tau_y$ $\Gamma_6:(\tau_z,-\tau_x)$
$\mathbf{H}^{5,6}$	$\Gamma_5\otimes\Gamma_6^*=\Gamma_3\oplus\Gamma_4\oplus\Gamma_5$	$\Gamma_3:-\tau_y$ $\Gamma_4:\mathbb{I}_{2\times2}$ $\Gamma_5:(\tau_x,\tau_z)$

The symmetrized matrices for every block of the $\mathbf{k}\cdot\mathbf{p}$ Hamiltonian are listed in Table II, where

$$\tau_x\equiv\begin{bmatrix}0&1\\1&0\end{bmatrix},\quad \tau_y\equiv\begin{bmatrix}0&-i\\i&0\end{bmatrix},\quad \tau_z\equiv\begin{bmatrix}1&0\\0&-1\end{bmatrix}$$

are Pauli matrices acting on the orbital band-edge Bloch functions. The irreducible tensor operators can be constructed from ordinary vector operators or axial vector operators by utilizing the last column of Table I and $R_xR_x'+R_yR_y'\sim zR_z$, $R_xR_y'-R_yR_x'\sim z$, $(R_yR_y'-R_xR_x',R_xR_y'+R_yR_x')\sim(R_x,R_y)$, where (R_x,R_y) and (R_x',R_y') transform according to Γ_5. From Table II, we see that $\mathbf{H}^{1,1}$ (i.e., $\mathbf{H}^{1c,1c}$,$\mathbf{H}^{1v,1v}$,$\mathbf{H}^{1c,1v}$, and $\mathbf{H}^{1v,1c}$) and $\mathbf{H}^{4,4}$ have the same symmetrized matrix that transform according to the same irreducible representation, so they always have exactly the same invariants. Similarly, $\mathbf{H}^{1,5}$ and $\mathbf{H}^{4,6}$ have exactly the same invariants; $\mathbf{H}^{1,6}$ and $\mathbf{H}^{4,5}$ have exactly the same invariants; and $\mathbf{H}^{5,5}$ and $\mathbf{H}^{6,6}$ have exactly the same invariants.

B. $\mathbf{k}\cdot\mathbf{p}$ Hamiltonian

In the absence of SOC, external field, and strain, only the 2D momentum operator $\mathbf{k}\equiv(k_x,k_y)$ can appear in the $\mathbf{k}\cdot\mathbf{p}$ Hamiltonian of the monolayer XSe. Since $[k_x,k_y]=0$, only three irreducible tensor operators can be constructed up to $O(k^2)$: $(k_x,k_y)\sim(x,y)$, $k_x^2+k_y^2\sim1$, and $(k_y^2-k_x^2,2k_xk_y)\sim(x,y)$. Under time reversal, the first one is odd, while the latter two are even. By combining them with the symmetrized matrices in Table II, we can readily obtain all the invariants for each block of the $\mathbf{k}\cdot\mathbf{p}$ Hamiltonian. The nonzero invariants up to $O(k^2)$ are listed in Table III. Note that according to Table II, we can construct another invariant $ik_x\tau_z-ik_y\tau_x$ for $\mathbf{H}^{5,5}$ and $\mathbf{H}^{6,6}$. Although this invariant obeys the D_{3h} symmetry and the time-reversal symmetry, it is not Hermitian, so it cannot be

TABLE III. Invariants for each block of the $\mathbf{k}\cdot\mathbf{p}$ Hamiltonian constructed from the 2D momentum operator up to the second order or from the strain tensor up to the first order. Here $k^2 \equiv k_x^2 + k_y^2$, τ_x, τ_y, τ_z are Pauli matrices acting on the orbital band-edge Bloch states, $\mathbf{H}^{1,1}$ stands for $\mathbf{H}^{1c,1c}$,$\mathbf{H}^{1v,1v}$,$\mathbf{H}^{1c,1v}$,$\mathbf{H}^{1v,1c}$, and $\mathbf{H}^{1,6}$ stands for $\mathbf{H}^{1c,6}$,$\mathbf{H}^{1v,6}$. The imaginary factor i ensures that all the invariants remain invariant under time reversal.

$\mathbf{H}^{1,1}$, $\mathbf{H}^{4,4}$	$\mathbf{H}^{5,5}$,$\mathbf{H}^{6,6}$	$\mathbf{H}^{1,6}$,$\mathbf{H}^{4,5}$
	$k^2\mathbb{I}_{2\times 2}$	$ik_x\Lambda_+ + ik_y\Lambda_-$
k^2		
	$(k_y^2 - k_x^2)\tau_z - 2k_xk_y\tau_x$	$(k_y^2 - k_x^2)\Lambda_+ + 2k_xk_y\Lambda_-$
	$(\epsilon_{xx} + \epsilon_{yy})\mathbb{I}_{2\times 2}$	
$\epsilon_{xx} + \epsilon_{yy}$		$(\epsilon_{yy} - \epsilon_{xx})\Lambda_+ + 2\epsilon_{xy}\Lambda_-$
	$(\epsilon_{yy} - \epsilon_{xx})\tau_z - 2\epsilon_{xy}\tau_x$	

used for the diagonal blocks $\mathbf{H}^{5,5}$ and $\mathbf{H}^{6,6}$ and hence does not appear in Table III. The general expression of each block of the $\mathbf{k}\cdot\mathbf{p}$ Hamiltonian is the linear combination (with real coefficients) of their corresponding invariants. Interestingly, the coupling $\mathbf{H}^{e-o} = (\mathbf{H}^{o-e})^\dagger$ between the even-parity and odd-parity states under the mirror reflection σ_h vanishes to all orders of k, because Table II shows that no irreducible operator transforming according to Γ_4 can be constructed out of k_x and k_y up to all orders. Consequently, the $\mathbf{k}\cdot\mathbf{p}$ Hamiltonian assumes the block-diagonal form:

$$\mathbf{H}_{\mathbf{k}\cdot\mathbf{p}} = \mathrm{diag}\left\{E_1^c, E_1^v, E_6^v, E_6^v, E_4^c, E_5^v, E_5^v\right\} + \mathrm{diag}\{\mathbf{H}^{e-e}, \mathbf{H}^{o-o}\}, \tag{4}$$

where $E_1^c, \ldots, E_5^v$ are band-edge energies, and

$$\mathbf{H}^{e-e} = \begin{bmatrix} Fk^2 & b_{11}^{vc}k^2 & ib_{61}^{vc}k_x & ib_{61}^{vc}k_y \\ & Mk^2 & ib_{61}^{vv}k_x & ib_{61}^{vv}k_y \\ & & Ck^2 + D\left(k_y^2 - k_x^2\right) & -2Dk_xk_y \\ & & & Ck^2 - D\left(k_y^2 - k_x^2\right) \end{bmatrix}, \tag{5}$$

$$\mathbf{H}^{o-o} = \begin{bmatrix} Gk^2 & ib_{54}^{vc}k_x & ib_{54}^{vc}k_y \\ & Ak^2 + B\left(k_y^2 - k_x^2\right) & -2Bk_xk_y \\ & & Ak^2 - B\left(k_y^2 - k_x^2\right) \end{bmatrix}. \tag{6}$$

In the above we only keep the lowest-order contribution to each matrix element, and only give the matrix elements in the upper triangle since the $\mathbf{k}\cdot\mathbf{p}$ Hamiltonian is Hermitian. Altogether there are 16 real parameters, including five band-edge energies and 11 coefficients A, B, C, D, F, G, M, b_{11}^{vc}, b_{61}^{vc}, b_{61}^{vv}, b_{54}^{vc} associated with the $\mathbf{k}$-dependent invariants.

All these parameters can be determined by comparing the energy band structure obtained from the $\mathbf{k}\cdot\mathbf{p}$ Hamiltonian to the first-principles calculations in the vicinity of the Γ point. The first-principles calculations detail is given in Appendix A. The parameters $E_1^c, \ldots, E_5^v$ are just the band-edge energies of the first-principles results at the Γ point. According to the first-principles calculations, the energy dispersion in the vicinity of the Γ point ($k < 0.1/\text{Å}$) is nearly isotropic, with the energy

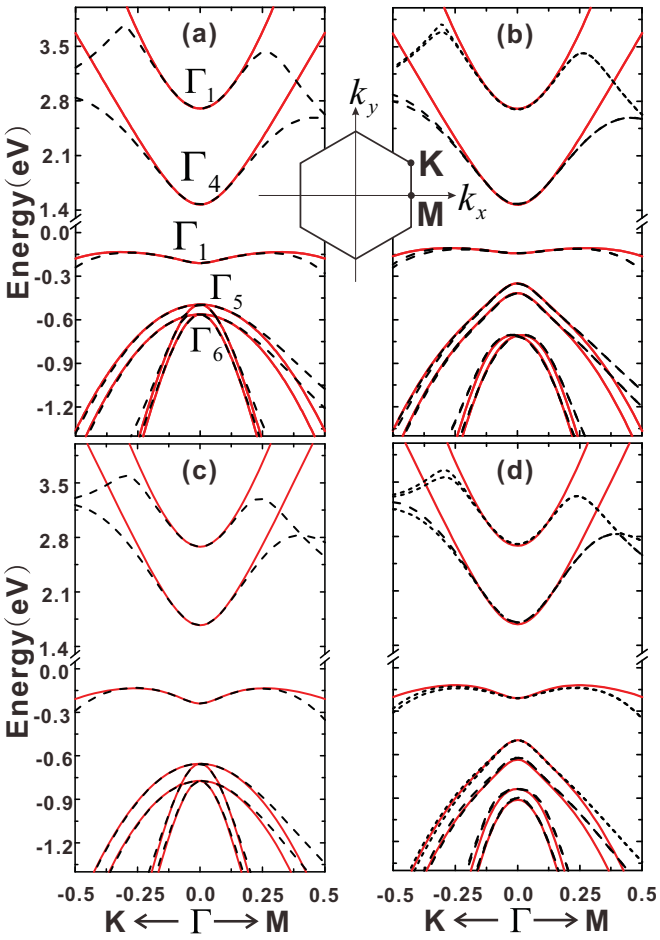

FIG. 2. The energy band structures of monolayer InSe in the (a) absence or (b) presence of SOC. (c) and (d): the same as (a) and (b), but for monolayer GaSe. The red solid (black dashed) lines are obtained from the $\mathbf{k}\cdot\mathbf{p}$ Hamiltonian in Eq. (4) (the first-principles calculations).

difference along the Γ-K and Γ-M directions being less than 1 meV. Performing the least square fitting within this range, we obtain the 11 coefficients associated with the $\mathbf{k}$-dependent invariants [40–47]. All the parameters in the $\mathbf{k}\cdot\mathbf{p}$ Hamiltonian are listed in Table VI and the comparison between the results from the $\mathbf{k}\cdot\mathbf{p}$ Hamiltonian (the red solid lines) and the first-principles calculations (the black dashed lines) are shown in Figs. 2(a) and 2(c). The detailed information about the first-principles calculations can be found in Appendix A.

Let us focus on the topmost valence band in Fig. 2(a). Our $\mathbf{k}\cdot\mathbf{p}$ Hamiltonian captures the sombrero dispersion—a most interesting feature of the monolayer InSe that may exhibit unconventional transport and optical properties. Specifically, the valence band maxima obtained from first-principles calculations locate away from the Γ point: along the Γ-K direction, it locates at $k = -0.29/\text{Å}$ and has an energy $E = -0.1372$ eV, while along the Γ-M direction, it locates at $k = 0.27/\text{Å}$ and has an energy $E = -0.1401$ eV. These features are well reproduced by our $\mathbf{k}\cdot\mathbf{p}$ model: the maximal deviation is less than 1 meV for k up to $0.2/\text{Å}$; and less than 5 meV for k up to $0.3/\text{Å}$ along the Γ-K direction. The difference

TABLE IV. Nonzero $\mathbf{k}\cdot\mathbf{p}$ parameters in the monolayer InSe (GaSe) $\mathbf{k}\cdot\mathbf{p}$ Hamiltonian.

Parameter	Value	Unit	Parameter	Value	Unit
E_1^c	2.7036	eV	E_4^c	1.4730	eV
	(2.68)			(1.67)	
E_1^v	−0.2090	eV	E_5^v	−0.4949	eV
	(−0.2382)			(−0.6545)	
E_6^v	−0.5626	eV	F	6.52	eV Å^2
	(–0.773)			(4.66)	
A	−2.06	eV Å^2	B	−1.41	eV Å^2
	(−2.56)			(−1.58)	
C	−3.87	eV Å^2	D	−0.11	eV Å^2
	(−3.78)			(−0.94)	
M	−1.45	eV Å^2	G	−0.72	eV Å^2
	(−2.09)			(−0.52)	
b_{54}^{vc}	−6.41	eV Å	b_{11}^{vc}	−4.95	eV Å^2
	(−7.63)			(−2.59)	
b_{61}^{vv}	1.49	eV Å	b_{61}^{vc}	6.38	eV Å
	(2.41)			(7.70)	
$\lambda_{5,5}$	0.1457	eV	$\lambda_{6,6}$	0.1467	eV Å
	(0.1541)			(−0.1388)	
$\lambda_{1_v,5}$	0.1299	eV			
	(0.0918)				

between the band structures obtained from the $\mathbf{k}\cdot\mathbf{p}$ theory and first-principles calculations becomes significant for the second conduction band (Γ_1) in the presence (absence) of the SOC.

Using the same $\mathbf{k}\cdot\mathbf{p}$ Hamiltonian with the parameters listed in the bracket in Table IV, we obtain the band structures of the GaSe monolayer in Fig. 2(c). As we can see, the sombrero dispersion also appears in Fig. 2(c) and was captured by our $\mathbf{k}\cdot\mathbf{p}$ Hamiltonian with an alternative set of values.

C. Spin-orbit coupling

For InSe monolayers, the SOC must be included since it induces large splitting of the Γ_5 and Γ_6 valences bands (of the order 0.3 eV according to our first-principles calculations). In the presence of SOC, the spin operator $\mathbf{s}=(s_x,s_y,s_z)$ can appear in the $\mathbf{k}\cdot\mathbf{p}$ Hamiltonian [48]. Since $\mathbf{s}$ is an axial vector, we have $(s_x,s_y)\sim(R_x,R_y)$ and $s_z\sim R_z$ under D_{3h} operations. The nonzero invariants constructed from the electron spin operator alone are listed in Table V. Since $\mathbf{H}^{1_c,5}$ and $\mathbf{H}^{4,6}$ are the coupling between the conduction bands and valence bands, their effects on the energy band dispersion is negligible.

TABLE V. Invariants for each block of the $\mathbf{k}\cdot\mathbf{p}$ Hamiltonian constructed from the electron spin operator $\mathbf{s}\equiv(s_x,s_y,s_z)$. Here $\mathbf{H}^{1,5}$ stands for $\mathbf{H}^{1c,5},\mathbf{H}^{1v,5}$. The imaginary factor i ensures that all the invariants remain invariant under time reversal.

$\mathbf{H}^{5,5}$, $\mathbf{H}^{6,6}$	$\mathbf{H}^{1,5}$,$\mathbf{H}^{4,6}$	$\mathbf{H}^{5,6}$
$\tau_y s_z$	$i\Lambda_- s_x - i\Lambda_+ s_y$	$i\tau_x s_x + i\tau_z s_y$

TABLE VI. Orbital analysis of the Perdew-Burke-Ernzerhof (PBE) bands at the Γ point. The labels $\Gamma_{5,1},\Gamma_{5,2},\Gamma_{6,1},\Gamma_{6,2}$ correspond to the second and third double degenerate valence bands.

	p_y	p_z	p_x	d_{xy}	d_{yz}	d_{z^2}	d_{xz}	d_{x^2}
$\Gamma_{5,1}$	0.483	0.000	0.162	0.010	0.016	0.000	0.005	0.031
$\Gamma_{5,2}$	0.162	0.000	0.483	0.031	0.005	0.000	0.016	0.010
$\Gamma_{6,1}$	0.492	0.000	0.165	0.010	0.011	0.000	0.004	0.031
$\Gamma_{6,2}$	0.165	0.000	0.492	0.031	0.004	0.000	0.011	0.010

Moreover, as shown in Table VI, the major composition of the Γ_5 and Γ_6 valence bands at the Γ point is the (p_x,p_y) atomic orbitals from each atom. However, the microscopic spin-orbit coupling Hamiltonian for each atom *alone* has no spin-flip term ($\propto s_x$ and s_y) between the (p_x,p_y) atomic orbitals. Thus the spin-flip invariant $i\tau_x s_x + i\tau_z s_y$ for $\mathbf{H}^{5,6}$ must come from either the interatomic contributions or the mixture of d orbitals into the Γ_5 and Γ_6 bands, both of which are very small (see Table VI). Therefore, we can safely neglect $\mathbf{H}^{5,6}$ and keep only three nonzero blocks for the SOC Hamiltonian $\mathbf{H}_{\rm soc}$: $\mathbf{H}_{\rm soc}^{5,5}=\lambda_{55}\tau_y\hat{s}_z$, $\mathbf{H}_{\rm soc}^{6,6}=\lambda_{66}\tau_y\hat{s}_z$, and $\mathbf{H}_{\rm soc}^{1v,5}=\lambda_{1_v5}(i\Lambda_- s_x - i\Lambda_+ s_y)$. The distinguishing feature of $\mathbf{H}_{\rm soc}$ compared with $\mathbf{H}_{\mathbf{k}\cdot\mathbf{p}}$ in Eq. (4) is that the invariant $i\Lambda_- s_x - i\Lambda_+ s_y$ couples the even-parity band-edge Bloch states $|\Psi_1\rangle,|\Psi_6\rangle$ to the odd-parity band-edge Bloch states $|\Psi_4\rangle,|\Psi_5\rangle$ under the σ_h operation. The coupling between $|\Psi_{1v}\rangle$ and the $|\Psi_5\rangle$ may push the Γ_1 valence band upwards at the Γ point.

$\mathbf{H}_{\rm soc}$ contains three real coefficients $\lambda_{55},\lambda_{66},\lambda_{1_v5}$. By comparing the band-edge energies from the $\mathbf{k}\cdot\mathbf{p}$ model to the first-principles results, we find that they have similar magnitudes (see Table IV). A detailed calculation of SOC parameters $\lambda_{55},\lambda_{66},\lambda_{1_v5}$ is given in Appendix B. In Fig. 2(b), we compare the results from the $\mathbf{k}\cdot\mathbf{p}$ model (red solid lines) and results (black dashed lines) from first-principles calculations including the SOC. As we can see, our model give a good description for the large energy splitting in the valence band induced by the SOC.

In principle, it is possible to construct other irreducible operators and hence invariants by combining the momentum operators (k_x,k_y) and the spin operators (s_x,s_y,s_z). For example, let $K_x=k_y^2-k_x^2$ and $K_y=2k_xk_y$. According to Table I, we have $k_xK_y-k_yK_x=3k_x^2k_y-k_y^3\sim R_z$ and hence $(3k_x^2k_y-k_y^3)s_z\sim 1$ under D_{3h} operations. Using Table II, we immediately obtain the invariants $(3k_x^2k_y-k_y^3)s_z$ for $\mathbf{H}_{\rm soc}^{1,1}$ and $(3k_x^2k_y-k_y^3)s_z\mathbb{I}_{2\times2}$ for $\mathbf{H}_{\rm soc}^{5,5}$ and $\mathbf{H}_{\rm soc}^{6,6}$. However, these invariants are higher order terms which only lead to a small splitting ($\sim$ a few meV) of the energy bands; hence these terms can safely be neglected. These analysis about the SOC effect also applies to GaSe monolayer. In Fig. 2(d) we compare the results from the $\mathbf{k}\cdot\mathbf{p}$ Hamiltonian (red solid lines) and GaSe monolayer band structure (black dashed lines) from first-principles calculations including the SOC.

III. INDIRECT-TO-DIRECT BAND-GAP TRANSITION

Strain engineering is an efficient and commonly used way to manipulate the electronic structures in two-dimensional materials, such as graphene, MoS_2, and black phosphorus, as

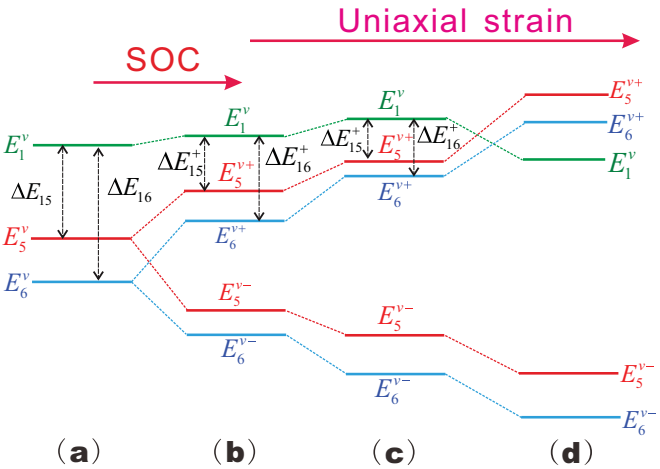

FIG. 3. Splitting of the valence band energy levels at the Γ point due to SOC and uniaxial strain: (a) No SOC and no strain. (b) SOC only. (c) SOC and small strain. (d) SOC and large strain.

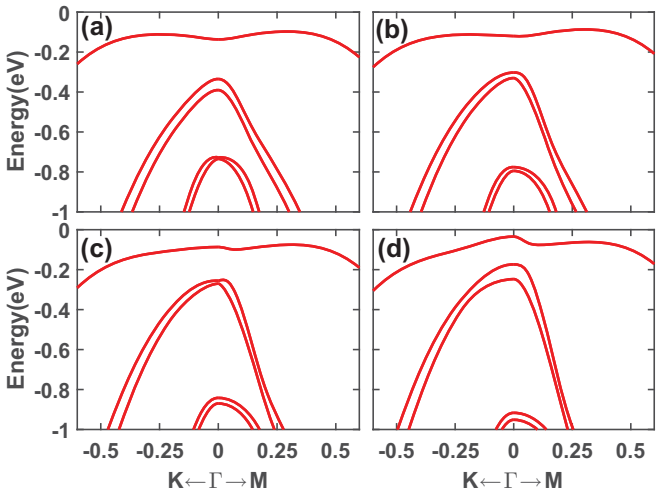

FIG. 4. Electronic band valence structures obtained from the $\mathbf{k}\cdot\mathbf{p}$ theory under uniaxial strains: (a) $\epsilon = 0.09$, (b) $\epsilon = 0.18$, (c) $\epsilon = 0.27$, and (d) $\epsilon = 0.36$.

these atomically thin membranes can withstand unprecedented strains of up to 10 to 25% without plastically deforming or rupturing [49–59]. In this section we study the effect of in-plane strain on the electronic structure of monolayer InSe. The in-plane strain is characterized by the tensor components $\epsilon_{xx}, \epsilon_{yy}, \epsilon_{xy} = \epsilon_{yx}$, which can be recombined into irreducible tensors: $\epsilon_{xx} + \epsilon_{yy} \sim 1$ and $(\epsilon_{yy} - \epsilon_{xx}, 2\epsilon_{xy}) \sim (x, y)$ under D_{3h} operations. Then we can use Table II to construct the strain invariants up to the first order, as listed in Table III. Here we consider uniaxial strain with $\epsilon_{xx} + \epsilon_{yy} = 0$, so we obtain two distinct invariants: $\mathbf{I}_1 = (\epsilon_{yy} - \epsilon_{xx})\tau_z - 2\epsilon_{xy}\tau_x$ for $\mathbf{H}^{5,5}$ and $\mathbf{H}^{6,6}$ and $\mathbf{I}_2 = (\epsilon_{yy} - \epsilon_{xx})\Lambda_+ + 2\epsilon_{xy}\Lambda_-$ for $\mathbf{H}^{1v,6}$, $\mathbf{H}^{1c,6}$ and $\mathbf{H}^{4,5}$. However, $\mathbf{H}^{1c,6}$ and $\mathbf{H}^{4,5}$ can be neglected since they describe coupling between the conduction and valence bands and hence have a very small effect on the energy band dispersion. Therefore, the uniaxial strain Hamiltonian $\mathbf{H}_{\text{strain}}$ only has three nonzero blocks: $\mathbf{H}^{5,5}_{\text{strain}} = \beta_{55}\mathbf{I}_1$, $\mathbf{H}^{6,6}_{\text{strain}} = \beta_{66}\mathbf{I}_1$, and $\mathbf{H}^{1v,6}_{\text{strain}} = \beta_{1v,6}\mathbf{I}_2$. In the presence of both SOC and strain, the total Hamiltonian is the sum of $\mathbf{H}_{\mathbf{k}\cdot\mathbf{p}}$ in Eq. (4), the SOC Hamiltonian $\mathbf{H}_{\text{soc}}$, and the strain Hamiltonian $\mathbf{H}_{\text{strain}}$.

Now we discuss qualitatively the effects of SOC and uniaxial strain on the band-edge energies at the Γ point. For simplicity we neglect the interband coupling $\mathbf{H}^{1v,5}_{\text{soc}}$ and $\mathbf{H}^{1v,6}_{\text{strain}}$ as the level splitting is dominated by the intraband coupling within the Γ_5 and Γ_6 bands. Due to the SOC and strain, the three valence band-edge energy levels E^v_1, E^v_5, and E^v_6 split into five levels E^v_1, E^{v+}_5, E^{v-}_5, E^{v+}_6, and E^{v-}_6 as shown in Figs. 3(b) and 3(c), where

$$E^{v\pm}_\eta = E^v_\eta \pm \sqrt{[\beta_{\eta\eta}(\epsilon_{yy} - \epsilon_{xx})]^2 + (2\epsilon_{xy}\beta_{\eta\eta})^2 + (\lambda_{\eta\eta})^2},$$

where $\eta = 5,6$. Thus the uniaxial strain and shear strain which can be described by the strain tensors $\epsilon_{yy} - \epsilon_{xx}$ and ϵ_{xy} can induce large splitting of the Γ_5 and Γ_6 valence bands, as sketched in Fig. 3. In particular, under a large uniaxial strain, the order of Γ_1, Γ_5, and Γ_6 valence band will be reversed as shown in Fig. 3(d).

For a quantitative study, we consider the uniaxial strain applied along the zigzag direction and take $\beta_{66}(\epsilon_{yy} - \epsilon_{xx}) \approx \beta_{55}(\epsilon_{yy} - \epsilon_{xx}) = \epsilon$. The energy dispersions of the valence bands under different uniaxial strain obtained from the $\mathbf{k}\cdot\mathbf{p}$ Hamiltonian are shown in Fig. 4. We see that uniaxial strain not only enhances the anisotropy of the energy dispersion along the Γ-K direction and Γ-M directions, but also reduces the energy difference among the top three valence bands. Interestingly, Fig. 4(d) shows a direct band gap character with the valence band top at the Γ point, as a result of the energy level inversion sketched in Fig. 3(d). Therefore, large uniaxial strain can induce a indirect-to-direct band gap transition.

This indirect-to-direct band gap transition is further confirmed by our first-principles results in Fig. 5. In the absence of strain [Fig. 5(a)], the topmost valence band states at the Γ point are dominated by the p_z antibonding states, while the

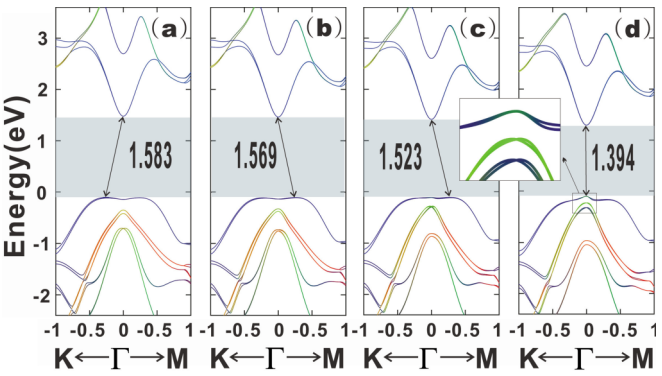

FIG. 5. Projected energy band structure of monolayer InSe with different uniaxial tensile strains along the zigzag direction: $\epsilon_{yy} - \epsilon_{xx}$ = (a) 0, (b) 3, (c) 6, and (d) 9%. The Fermi level is set to be 0 eV. In the projected band structure, the states dominated by p_x, p_y, and p_z orbitals are plotted in red, green, and blue. All the results are obtained from the density-functional theory (DFT) with the PBE functional adopted. (See Appendix A.) The energy gap is shaded by the gray rectangles, and the values (in eV) obtained with PBE are given.

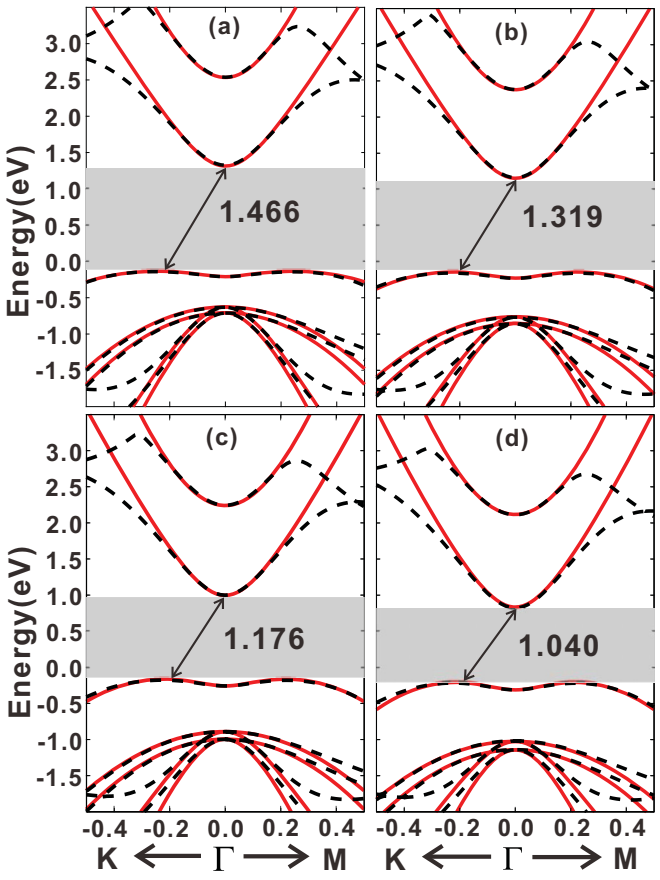

FIG. 6. The electronic band structures under different biaxial strains (a) 1, (b) 2, (c) 3, and (d) 4%. The red solid lines correspond to results obtained from our $\mathbf{k}\cdot\mathbf{p}$ model, while the black dashed lines are energy bands for biaxial strained InSe obtained from the DFT with the PBE functional adopted.

lowest conduction band states at the Γ point are dominated by p_z bonding states. For the second and third valence bands, the states at the Γ point are mainly derived from $p_x \pm ip_y$ states. An indirect band gap is clearly visible in the band structures where the valence band top is about 0.29/Å away from the Γ point. As shown in Figs. 5(b) to 5(d), uniaxial strain can not only enhances the anisotropy between the energy dispersion along different directions, but also decrease the band gap. Furthermore, the InSe monolayer experiences a transition from an indirect band gap to a direct gap when subjected to large uniaxial tensile strain, $\epsilon_{yy} - \epsilon_{xx} = 9\%$ as shown in Fig. 5(d). It is clearly seen from the inset of Fig. 5(d) that under strong uniaxial strain, the topmost valence band states at the Γ point are dominated not by the p_z orbital but instead by the p_y orbital. The third highest valence band state is dominated by the p_z orbital instead of the p_y orbital, consistent with the energy level inversion in Fig. 3(d).

Finally we briefly discuss the effect of biaxial strain on the electronic band structure of monolayer InSe based on first-principles calculations. As shown in Fig. 6, in the presence of biaxial tensile strain along the x (armchair) and y (zigzag) directions, the indirect band gap is reduced to 1.04 eV under 4% tensile biaxial strain. The biaxial tensile strain also significantly increases the separation between different valence bands, which may affect the transport properties of p-doped monolayer InSe. Since monolayer InSe has mirror symmetry σ_h (see Table I), optical absorption occurs between the lowest conduction band and the second highest valence band. In the presence of biaxial strain, the lowest conduction band drops faster than second highest valence band. This leads to a red shift of the optical absorption. These properties also captured by our multiband $\mathbf{k}\cdot\mathbf{p}$ Hamiltonian $\mathbf{H} = \mathbf{H}_{\mathbf{k}\cdot\mathbf{p}} + \mathbf{H}_{\mathbf{bistr}}$. The additional biaxial strain induced Hamiltonian $\mathbf{H}_{\mathbf{bistr}}$ also follows the block-diagonal form:

$$\begin{aligned}\mathbf{H}_{\mathbf{bistr}} = {} & \mathrm{diag}\{\gamma_1^c\epsilon, \gamma_1^v\epsilon, \gamma_6^v\epsilon, \gamma_6^v\epsilon, \gamma_4^c\epsilon, \gamma_5^v\epsilon, \gamma_5^v\epsilon\} \\ & + \mathrm{diag}\{\mathbf{H}_{\mathbf{bistr}}^{\mathrm{e-e}}, \mathbf{H}_{\mathbf{bistr}}^{\mathrm{o-o}}\},\end{aligned} \tag{7}$$

where $\epsilon = \epsilon_{xx} + \epsilon_{yy}$ is the biaxial strain, and

$$\mathbf{H}_{\mathbf{bistr}}^{\mathrm{e-e}} = \begin{bmatrix} \gamma_F\epsilon k^2 & \Delta\epsilon + \gamma_{11}^{vc}\epsilon k^2 & i\gamma_{61}^{vc}\epsilon k_x & i\gamma_{61}^{vc}\epsilon k_y \\ & \gamma_M\epsilon k^2 & i\gamma_{61}^{vv}\epsilon k_x & i\gamma_{61}^{vv}\epsilon k_y \\ & & \gamma_C\epsilon k^2 + \gamma_D\epsilon k_-^2 & -2\gamma_D\epsilon k_x k_y \\ & & & \gamma_C\epsilon k^2 - \gamma_D\epsilon k_-^2 \end{bmatrix}, \tag{8}$$

$$\mathbf{H}_{\mathbf{bistr}}^{\mathrm{o-o}} = \begin{bmatrix} \gamma_G\epsilon k^2 & i\gamma_{54}^{vc}\epsilon k_x & i\gamma_{54}^{vc}\epsilon k_y \\ & \gamma_A\epsilon k^2 + \gamma_B\epsilon k_-^2 & -2\gamma_B\epsilon ksc132_x k_y \\ & & \gamma_A\epsilon k^2 - \gamma_B\epsilon k_-^2 \end{bmatrix}. \tag{9}$$

where $k_-^2 = k_y^2 - k_x^2$. Since the biaxial strain $\epsilon = \epsilon_{xx} + \epsilon_{yy}$ belongs to the Γ_1 irreducible representation, the products of ϵ and any invariants in Eqs. (4)–(6) are also invariant. Therefore, all the biaxial strain induced terms $\{\gamma_F\epsilon, \gamma_M\epsilon, \gamma_{11}^{vc}\epsilon, \ldots\}$ can be considered as modifications of $\mathbf{k}\cdot\mathbf{p}$ parameters shown in Table IV except for $\Delta\epsilon$. The reason why $\Delta\epsilon$ occurs is that Γ_1 is a direct product of the Γ_1 valence band block state $|\Psi_{1v}\rangle$ and the Γ_1 conduction band block state $|\Psi_{1c}\rangle$ ($\Gamma_1 = \Gamma_1 \otimes \Gamma_1$).

By fitting the band structure obtained from the $\mathbf{k}\cdot\mathbf{p}$ Hamiltonian with the band structure obtained from the DFT with the PBE functional adopted, we finally obtain all the biaxial strain dependent parameters shown in Table VII. The comparison between the results from the $\mathbf{k}\cdot\mathbf{p}$ Hamiltonian (the red solid line) and the first-principles calculation (the black dashed line) are shown in Fig. 6. The biaxial strain $\mathbf{k}\cdot\mathbf{p}$ Hamiltonian shows that the energy of the optical absorption

TABLE VII. Nonzero biaxial strain dependent parameters in the monolayer InSe Hamiltonian.

Parameter	Value	Unit	Parameter	Value	Unit
γ_1^c	−17.67	eV	γ_4^c	−15.90	eV
γ_1^v	0.52	eV	γ_5^v	−13.20	eV
γ_6^v	−14.43	eV	γ_F	12.23	eV Å^2
γ_A	7.60	eV Å^2	γ_B	−0.72	eV Å^2
γ_C	−3.56	eV Å^2	γ_D	6.90	eV Å^2
γ_M	−112.99	eV Å^2	γ_G	97.45	eV Å^2
γ_{54}^{vc}	10.33	eV Å	γ_{11}^{vc}	−82.79	eV Å^2
γ_{61}^{vv}	30.45	eV Å	γ_{61}^{vc}	−41.53	eV Å
Δ	−13.24	eV			

due to transitions from the second highest valence band to the lowest conduction band can be tuned by the biaxial strain: $E_{\mathbf{ab}} = E_4^c - E_5^v + (\gamma_4^c - \gamma_5^v)\epsilon = E_4^c - E_5^v - 2.7\epsilon$.

IV. CONCLUSION

We have adopted the standard invariant theory to derive a 14-band (including the spin degree of freedom) Hamiltonian for the electronic structure of the XSe (X = In, Ga) monolayer including the strain effects. Our model can describe not only the nonparabolic energy band dispersion of the valence bands, but also the strong interband mixing and strain effects. The $\mathbf{k}\cdot\mathbf{p}$ Hamiltonian recovers the sombrero dispersion of the top valence band of InSe and agrees well with the first-principles results for wave vector $k \leqslant 0.3/\text{Å}$. We further predict that a large uniaxial strain can change the indirect band gap of InSe to a direct band gap. Our $\mathbf{k}\cdot\mathbf{p}$ model may provides a simple and systematic method to understand and manipulate the electronic and optical properties of monolayer XSe and their nanostructures by strain and various external fields. Our multiband model can also be extended to few-layer systems.

ACKNOWLEDGMENTS

This work was supported by the MOST of China (Grants No. 2017YFA0303400, No. 2016YFE0110000, and No. 2015CB921503), the NSFC of China (Grants No. 11434010, No. 61674145, No. 11574303, No. 11274036, and No. 11322542) and the Chinese Academy of Sciences (Grants No. QYZDJ-SSW-SYS001 and No. XDPB0603).

APPENDIX A: THE DETAILED INFORMATION OF THE FIRST-PRINCIPLES CALCULATIONS

For monolayer XSe, we use the Vienna *ab initio* simulation package (VASP) [60] within the generalized gradient approximation (GGA) in the PBE [61] type and the projector augmented-wave (PAW) pseudopotential [62]. We set the kinetic energy cutoff to 500 eV for the wave function expansion and the k-point grid is sampled by sums over $9\times9\times1$ [63]. The electronic self-consistent calculations converge up to a precision of 10^{-6} eV in total energy difference. A slab model, together with a vacuum layer larger than 20 Å, is employed. During the structure optimization of monolayers InSe and GaSe, all atomic positions and lattice parameters are fully relaxed, and the maximum force allowed on each atom was less than 0.01 eV/Å. The calculated lattice parameter of the monolayer InSe is $a = 4.04$ Å. For monolayer GaSe, the lattice parameter is $a = 3.82$ Å. Our numerical results shown in Fig. 2 are in good agreement with the previous works (Refs. [30–32]).

APPENDIX B: THE SOC PARAMETERS FOR k · p HAMILTONIAN

In the presence of SOC, we can study the analytical expressions for energy eigenvalues at the Γ point. Assuming that $\mathbf{H}_{\text{soc}}$ has only three nonzero blocks: ($\mathbf{H}_{\text{soc}}^{5,5} = \lambda_{55}\tau_y\hat{s}_z$, $\mathbf{H}_{\text{soc}}^{6,6} = \lambda_{66}\tau_y\hat{s}_z$, and $\mathbf{H}_{\text{soc}}^{1_v,5} = \lambda_{1_v5}(i\Lambda_- s_x - i\Lambda_+ s_y)$), the Hamiltonian $\text{diag}\{E_1^c, E_1^v, E_6^v, E_6^c, E_4^c, E_5^v, E_5^v\} + \mathbf{H}_{\text{soc}}$ is easily diagonalized, and the eigenvalues are given as follows:

$$
\begin{aligned}
U_1 &= \frac{E_1^v + E_5^v - \lambda_{55}}{2} + \frac{\sqrt{\left(E_1^v - E_5^v + \lambda_{55}\right)^2 + 8(\lambda_{1_v5})^2}}{2},\\
U_2 &= \frac{E_1^v + E_5^v - \lambda_{55}}{2} - \frac{\sqrt{\left(E_1^v - E_5^v + \lambda_{55}\right)^2 + 8(\lambda_{1_v5})^2}}{2},\\
U_3 &= E_5^v + \lambda_{55},\\
U_4 &= E_6^v + \lambda_{66},\\
U_5 &= E_6^v - \lambda_{66}.
\end{aligned}
\tag{B1}
$$

Theoretically speaking, the SOC parameters contained in the above λ_{55},λ_{66}, and λ_{1_v5} could be obtained by solving the nonlinear equations. But the uncertain numerical relationship between eigenvalues U_1,U_2,U_3,U_4,U_5 would provide many kinds of possible solutions and further analysis would be necessary. To obtain the definite values of four SOC parameters contained in above equations, the following cases are considered: (I) $\lambda_{55} > 0$ and $\lambda_{66} > 0$ which lead to the relation $U_1 > U_3 > U_4 > U_2 > U_5$; (II) $\lambda_{55} > 0$ and $\lambda_{66} < 0$ which lead to the relation $U_1 > U_3 > U_5 > U_2 > U_4$; (III) $\lambda_{55} < 0$ and $\lambda_{66} > 0$ which lead to the relation $U_1 > U_2 > U_3 > U_4 > U_5$; and (IV) $\lambda_{55} < 0$ and $\lambda_{66} < 0$ which lead to the relation $U_1 > U_2 > U_5 > U_3 > U_4$. With SOC taken into account, the $\mathbf{k}\cdot\mathbf{p}$ model developed by case (III) or (IV) cannot fit to the first principles calculated band structure. Therefore, we finally obtain the InSe monolayer SOC parameter sets for case (I): $\lambda_{55} = 0.1451$,$\lambda_{6,6} = 0.1471$,$\lambda_{1_v5} = 0.1301$; and for case (II): $\lambda_{55} = 0.1451$,$\lambda_{66} = -0.1463$,$\lambda_{1_v5} = 0.1301$. For the GaSe monolayer, the SOC parameter sets are $\lambda_{55} = 0.1541$,$\lambda_{6,6} = 0.1388$, and $\lambda_{1_v5} = 0.0918$ in case (I); and $\lambda_{55} = 0.1541$,$\lambda_{6,6} = -0.1388$, and $\lambda_{1_v5} = 0.0918$ in case (II).

[1] A. H. C. Neto, F. Guinea, N. M. R. Peres, K. S. Novoselov, and A. K. Geim, Rev. Mod. Phys. **81**, 109 (2009).
[2] B. Radisavljevic, A. Radenovic, J. Brivio, V. Giacometti, and A. Kis, Nat. Nanotech **6**, 147 (2011).
[3] T. Cao, G. Wang, W. Han, H. Ye, C. Zhu, J. Shi, Q. Niu, P. Tan, E. Wang, B. Liu, and J. Feng, Nat. Commun. **3**, 887 (2012).
[4] K. F. Mak, K. He, J. Shan, and T. F. Heinz, Nat. Nanotech **7**, 494 (2012).

[5] Q. H. Wang, K. Kalantar-Zadeh, A. Kis, J. N. Coleman, and M. S. Strano, Nat. Nanotech **7**, 699 (2012).

[6] H. Zeng, J. Dai, W. Yao, D. Xiao, and X. Cui, Nat. Nanotech **7**, 490 (2012).

[7] D. Akinwande, N. Petrone, and J. Hone, Nat. Commun. **5**, 5678 (2014).

[8] G. Fiori, F. Bonaccorso, G. Iannaccone, T. Palacios, D. Neumaier, A. Seabaugh, S. K. Banerjee, and L. Colombo, Nat. Nanotech **9**, 768 (2014).

[9] L. Li, Y. Yu, G. J. Ye, Q. Ge, X. Ou, H. Wu, D. Feng, X. H. Chen, and Y. Zhang, Nat. Nanotech **9**, 372 (2014).

[10] R. A. Doganov, E. C. O'Farrell, S. P. Koenig, Y. Yeo, A. Ziletti, A. Carvalho, D. K. Campbell, D. F. Coker, K. Watanabe, T. Taniguchi, A. H. Castro Neto, and B. Ozyilmaz, Nat. Commun. **6**, 6647 (2015).

[11] D. A. Bandurin, A. V. Tyurnina, G. L. Yu, A. Mishchenko, V. Zolyomi, S. V. Morozov, R. K. Kumar, R. V. Gorbachev, Z. R. Kudrynskyi, S. Pezzini, Z. D. Kovalyuk, U. Zeitler, K. S. Novoselov, A. Patane, L. Eaves, I. V. Grigorieva, V. I. Fal'ko, A. K. Geim, and Y. Cao, Nat. Nanotechnol. **12**, 223 (2017).

[12] R. W. Damon and R. W. Redington, Phys. Rev. **96**, 1498 (1954).

[13] P. K. Larsen, S. Chiang, and N. V. Smith, Phys. Rev. B **15**, 3200 (1977).

[14] C. De Blasi, G. Micocci, A. Rizzo, and A. Tepore, Phys. Rev. B **27**, 2429 (1983).

[15] A. Khater, M. Balkanski, C. Julien, and M. Weber, Phys. Rev. B **37**, 8278 (1988).

[16] P. Gomes da Costa, M. Balkanski, and R. F. Wallis, Phys. Rev. B **43**, 7066 (1991).

[17] A. Segura, B. Marí, J. Martinez-Pastor, and A. Chevy, Phys. Rev. B **43**, 4953 (1991).

[18] P. Gomes da Costa, R. G. Dandrea, R. F. Wallis, and M. Balkanski, Phys. Rev. B **48**, 14135 (1993).

[19] M. O. D. Camara, A. Mauger, and I. Devos, Phys. Rev. B **65**, 125206 (2002).

[20] F. J. Manjón, A. Segura, V. Muñoz-Sanjosé, G. Tobías, P. Ordejón, and E. Canadell, Phys. Rev. B **70**, 125201 (2004).

[21] D. Errandonea, A. Segura, F. J. Manjón, A. Chevy, E. Machado, G. Tobias, P. Ordejón, and E. Canadell, Phys. Rev. B **71**, 125206 (2005).

[22] D. Errandonea, D. Martínez-García, A. Segura, J. Haines, E. Machado-Charry, E. Canadell, J. C. Chervin, and A. Chevy, Phys. Rev. B **77**, 045208 (2008).

[23] P. A. Hu, Z. Z. Wen, L. F. Wang, P. H. Tan, and K. Xiao, ACS Nano **6**, 5988 (2012).

[24] Y. B. Zhou, Y. F. Nie, Y. Liu, K. Yan, J. Hong, C. H. Jin, Y. Zhou, J. Yin, Z. F. Liu, and H. L. Peng, ACS Nano **8**, 1485 (2014).

[25] Y. D. Ma, Y. Dai, M. Guo, L. Yu, and B. B. Huang, Phys. Chem. Chem. Phys. **15**, 7098 (2013).

[26] D. J. Late, B. Liu, J. Luo, A. Yan, H. S. Matte, M. Grayson, C. N. Rao, and V. P. Dravid, Adv. Mat. **24**, 3549 (2012).

[27] S. Lei, L. Ge, Z. Liu, S. Najmaei, G. Shi, G. You, J. Lou, R. Vajtai, and P. M. Ajayan, Nano Lett. **13**, 2777 (2013).

[28] P. Hu, J. Zhang, M. Yoon, X.-F. Qiao, X. Zhang, W. Feng, P. Tan, W. Zheng, J. Liu, X. Wang, J. C. Idrobo, D. B. Geohegan, and K. Xiao, Nano Res. **7**, 694 (2014).

[29] S. Lei, X. Wang, B. Li, J. Kang, Y. He, A. George, L. Ge, Y. Gong, P. Dong, Z. Jin, G. Brunetto, W. Chen, Z. T. Lin, R. Baines, D. S. Galvao, J. Lou, E. Barrera, K. Banerjee, R. Vajtai, and P. Ajayan, Nat. Nanotech **11**, 465 (2016).

[30] H. L. Zhuang and R. G. Hennig, Chem. Mat. **25**, 3232 (2013).

[31] V. Zólyomi, N. D. Drummond, and V. I. Fal'ko, Phys. Rev. B **87**, 195403 (2013).

[32] D. V. Rybkovskiy, A. V. Osadchy, and E. D. Obraztsova, Phys. Rev. B **90**, 235302 (2014).

[33] P. Li and I. Appelbaum, Phys. Rev. B **92**, 195129 (2015).

[34] S. J. Magorrian, V. Zólyomi, and V. I. Fal'ko, Phys. Rev. B **94**, 245431 (2016).

[35] H. R. Trebin, U. Rössler, and R. Ranvaud, Phys. Rev. B **20**, 686 (1979).

[36] R. Winkler and U. Zülicke, Phys. Rev. B **82**, 245313 (2010).

[37] T. L. Linnik, J. Phys. Con. Mat. **24**, 205302 (2012).

[38] F. Geissler, J. C. Budich, and B. Trauzettel, New J. Phys. **15**, 085030 (2013).

[39] G. L. Bir and G. E. Pikus, *Symmetry and Strain-Induced Effects in Semiconductors* (Wiley, New York, 1974).

[40] P. Pfeffer and W. Zawadzki, Phys. Rev. B **53**, 12813 (1996).

[41] S. L. Chuang and C. S. Chang, Phys. Rev. B **54**, 2491 (1996).

[42] K. Kim, W. R. L. Lambrecht, B. Segall, and M. van Schilfgaarde, Phys. Rev. B **56**, 7363 (1997).

[43] D. J. Dugdale, S. Brand, and R. A. Abram, Phys. Rev. B **61**, 12933 (2000).

[44] M. Suzuki, T. Uenoyama, and A. Yanase, Phys. Rev. B **52**, 8132 (1995).

[45] P. Rinke, M. Winkelnkemper, A. Qteish, D. Bimberg, J. Neugebauer, and M. Scheffler, Phys. Rev. B **77**, 075202 (2008).

[46] A. Punya and W. R. L. Lambrecht, Phys. Rev. B **85**, 195147 (2012).

[47] P. E. Faria Junior, T. Campos, C. M. O. Bastos, M. Gmitra, J. Fabian, and G. M. Sipahi, Phys. Rev. B **93**, 235204 (2016).

[48] R. Winkler, *Spin-Orbit Coupling Effects in Two-Dimensional Electron and Hole Systems* (Springer, Berlin, 2003).

[49] F. Guinea, M. I. Katsnelson, and A. K. Geim, Nat. Phys. **6**, 30 (2009).

[50] N. Levy, S. A. Burke, K. L. Meaker, M. Panlasigui, A. Zettl, F. Guinea, A. H. Castro Neto, and M. F. Crommie, Science **329**, 544 (2010).

[51] C. C. Liu, W. Feng, and Y. Yao, Phys. Rev. Lett. **107**, 076802 (2011).

[52] F. de Juan, M. Sturla, and M. A. H. Vozmediano, Phys. Rev. Lett. **108**, 227205 (2012).

[53] M. A. Cazalilla, H. Ochoa, and F. Guinea, Phys. Rev. Lett. **113**, 077201 (2014).

[54] M. Elahi, K. Khaliji, S. M. Tabatabaei, M. Pourfath, and R. Asgari, Phys. Rev. B **91**, 115412 (2015).

[55] C. K. Gan and Y. Y. F. Liu, Phys. Rev. B **94**, 134303 (2016).

[56] C. Kamal, A. Chakrabarti, and M. Ezawa, Phys. Rev. B **93**, 125428 (2016).

[57] J.-H. Lin, H. Zhang, X.-L. Cheng, and Y. Miyamoto, Phys. Rev. B **94**, 195404 (2016).

[58] P. San-Jose, V. Parente, F. Guinea, R. Roldán, and E. Prada, Phys. Rev. X **6**, 031046 (2016).

[59] E. Taghizadeh Sisakht, F. Fazileh, M. H. Zare, M. Zarenia, and F. M. Peeters, Phys. Rev. B **94**, 085417 (2016).

[60] G. Kresse and J. Furthmüller, Phys. Rev. B **54**, 11169 (1996).

[61] J. P. Perdew, K. Burke, and M. Ernzerhof, Phys. Rev. Lett. **77**, 3865 (1996).

[62] P. E. Blochl, Phys. Rev. B **50**, 17953 (1994).

[63] H. J. Monkhorst and J. D. Pack, Phys. Rev. B **13**, 5188 (1976).